The Astrophysical Journal, 960:18 (9pp), 2024 January 1 https://doi.org/10.3847/1538-4357/ad0898
© 2023. The Author(s). Published by the American Astronomical Society.
OPEN ACCESS

ÆSOPUS 2.0: Low-temperature Opacities with Solid Grains

Paola Marigo[1], Peter Woitke[2], Emanuele Tognelli[3], Léo Girardi[4], Bernhard Aringer[5], and Alessandro Bressan[6]
[1] Department of Physics and Astronomy G. Galilei, University of Padova, Vicolo dell'Osservatorio 3, I-35122, Padova, Italy; paola.marigo@unipd.it
[2] Space Research Institute, Austrian Academy of Sciences, Schmiedlstr. 6, 8042, Graz, Austria
[3] CEICO, Institute of Physics of the Czech Academy of Sciences, Na Slovance 2, 182 21 Praha 8, Czech Republic
[4] INAF-Osservatorio Astronomico di Padova, Vicolo dell'Osservatorio 5, I-35122 Padova, Italy
[5] Department of Astrophysics, University of Vienna, Türkenschanzstrasse 17, A-1180 Vienna, Austria
[6] SISSA, via Bonomea 265, I-34136 Trieste, Italy
Received 2023 August 2; revised 2023 October 9; accepted 2023 October 30; published 2023 December 19

Abstract

In this study we compute the equation of state and Rosseland mean opacity from temperatures of $T \simeq 30{,}000$ K down to $T \simeq 400$ K, pushing the capabilities of the ÆSOPUS code into the regime where solid grains can form. The GGchem code is used to solve the chemistry for temperatures less than ≃3000 K. Atoms, molecules, and dust grains in thermodynamic equilibrium are all included in the equation of state. To incorporate monochromatic atomic and molecular cross sections, an optimized opacity sampling technique is used. The Mie theory is employed to calculate the opacity of 43 grain species. Tables of Rosseland mean opacities for scaled-solar compositions are provided. Based on our computing resources, opacities for other chemical patterns, as well as various grain sizes, porosities, and shapes, can be easily computed upon user request to the corresponding author.

Unified Astronomy Thesaurus concepts: Stellar atmospheric opacity (1585); Astrochemistry (75); Silicate grains (1456); Carbonaceous grains (201)

1. Introduction

One of the major theoretical tasks in modern astrophysics is to predict the elemental abundances and opacities in the atmospheres of stars, brown dwarfs, and planets. The interpretation of spectroscopic observations, in particular, necessitates thorough information on these two components. In recent years, technological advancements have enabled us to investigate the surface/circumstellar chemical composition and spectral features of evolved red giants such as asymptotic giant branch stars (Ramstedt & Olofsson 2014; Decin et al. 2017; Ramstedt et al. 2020), brown dwarfs (Allard et al. 1997; Marley 1997; Burrows et al. 1998; Cushing et al. 2008; Helling & Casewell 2014), and exoplanets (Fraine et al. 2014; Birkby et al. 2017), exploiting a wide range of wavelengths. The James Webb Space Telescope's infrared equipment is expected to transform our knowledge of these low-temperature objects (Beichman et al. 2014). In the future, PLATO (Rauer et al. 2016) will search for habitable, Earth-like planets by applying astroseismology to solar-like stars, for which modeling efforts to derive elemental abundances and opacities will be critical. The chemistry and opacity of the coolest objects must include the contribution of solid species, commonly referred to as dust grains, typically below $T \simeq 1500$ K.

The most used opacity tables that take into account dust grains are those of the Wichita State University group. Alexander (1975) computed opacities down to $T \simeq 700$ K, including a rough estimate of dust grain opacity, while better approximations were later introduced by Alexander & Ferguson (1994). Ferguson et al. (2005) made a significant advancement, using the PHOENIX code (Allard et al. 2001) to compute the abundances of solid grains in thermal equilibrium within the equation of state (EoS) solution. Other important efforts include Semenov et al. (2003)'s opacity tables for primary use in protoplanetary disk models, suitable for gas and dust mixtures ranging from $T \simeq 10$ K to $T \simeq 10{,}000$ K, and Freedman et al. (2008), who computed line and mean opacities, without the contribution of dust grains, for ultracool dwarfs and extrasolar planets in the temperature interval from $T \simeq 75$ K to $T \simeq 4000$ K.

In the field of low-temperature gas opacities, Marigo & Aringer (2009) constructed the ÆSOPUS code (Marigo & Aringer 2009, initial version ÆSOPUS 1.0), which solves the equation of state for over 800 chemical species (atoms/ions and molecules) and computes the Rosseland mean opacities for arbitrary chemical compositions under the assumption of thermodynamic equilibrium. Recently, Marigo et al. (2022, current version ÆSOPUS 2.0) made a major update to include new thermodynamic data (e.g., partition functions) and to expand molecular absorption to include 80 species, mostly taken from the ExoMol and HITRAN databases (Tennyson & Yurchenko 2012; Gordon et al. 2022). The reader should consult Marigo et al. (2022) for more information, particularly Tables 1 and 2 for a complete list of all opacity sources considered.

For both versions of ÆSOPUS, we set up a web interface[7] that enables users to compute in real time opacity tables based on their specific needs. The online service provides full control over the chemical abundances of 92 atomic species, ranging from hydrogen to uranium. Both EoS and opacity calculations are performed over a temperature range of $1500 \lesssim T/\mathrm{K} \lesssim 30{,}000$, with the chemistry of all components in the gas phase.

In this study we extend the computations to lower temperatures down to 100 K, where liquid and solid species appear and dominate both the EoS and the opacity. The EoS is solved using two codes: ÆSOPUS for temperatures $3000 \lesssim T/\mathrm{K} \lesssim 30{,}000$ (Marigo & Aringer 2009; Marigo et al. 2022) and GGchem for temperatures $100 \lesssim T/\mathrm{K} \lesssim 3000$ (Woitke et al. 2018). The latter takes into account grain condensation in

[7] http://stev.oapd.inaf.it/aesopus

Original content from this work may be used under the terms of the Creative Commons Attribution 4.0 licence. Any further distribution of this work must maintain attribution to the author(s) and the title of the work, journal citation and DOI.

thermal equilibrium with the gas phase. Low-temperature opacities are calculated using optical constants for a wide range of materials that condense in the coolest layers of stellar atmospheres and during star and planet formation.

New Rosseland mean opacity tables are provided here for scaled-solar abundances. They are built as a function of two standard parameters:

$$T \quad \text{and} \quad R = \rho T_6^{-3}, \tag{1}$$

where T is the temperature (in K) and the R parameter contains both the temperature ($T_6 = T/(10^6\,\mathrm{K})$) and the gas mass density ρ (in g cm^{-3}). We recall that using the R parameter instead of gas density ρ or pressure P enables the opacity tables to encompass rectangular areas of the (R, T) plane, resulting in an appropriate format for smooth opacity interpolation.

The Rosseland mean opacity tables and optical constants for dust species are available via the repository at http://stev.oapd.inaf.it/aesopus_2.0/tables; copies of these files have also been deposited to Zenodo: doi:10.5281/zenodo.8221361.

This paper is organized as follows. Section 2 details the method for solving the EoS. The opacity of solid grains is treated in Section 3 and in Table 1. Section 4 provides a thorough discussion of the Rosseland mean opacity and summarizes some important updates of molecular line absorption, with a focus on the temperature window where dust grains appear. Opacities for protoplanetary disks and chemical composition effects (for example, alpha-enhanced mixtures) are also investigated, along with a comparison to other available opacity data. The new opacity tables are introduced in Section 5. A few concluding remarks close the paper in Section 6.

2. Equation of State

The software program ÆSOPUS employs the ideal-gas assumption to solve the equation of state for over 800 species, including approximately 300 atoms and ions and 500 molecules, in the gas phase under conditions of thermodynamic and instantaneous chemical equilibrium. It encompasses the temperature range $1500 \lesssim T/\mathrm{K} \lesssim 30{,}000$. At low temperatures ($T \lesssim 2000$ K), the problem of determining the equilibrium chemical composition becomes more complex, as it entails also the formation of liquids and solids. In this regime we solve the EoS using the computer code GGchem (Woitke et al. 2018), which computes the abundances of roughly 568 gas molecules, 55 liquid species, and almost 200 solid particles. We set a transition temperature of ≃3000 K, below which we switch from ÆSOPUS to GGchem.

Figure 1 depicts the concentrations of a few molecules in the gas phase as a function of temperature. As we can see, the match between ÆSOPUS and GGchem is smooth and without discontinuities across the transition temperature. To better assess the differences in molecular abundances between ÆSOPUS and GGchem, we performed two independent runs of the codes in the temperature interval $3.3 \leqslant \log(T/\mathrm{K}) \leqslant 3.7$. We find that deviations in the predicted molecular concentrations typically range from a few 0.001 dex to a few 0.01 dex. This gives us confidence in the physical consistency of the two codes.

Additionally, it is important to examine the gas pressure that our opacity tables cover. Figure 2 provides an example. The chemical composition is scaled-solar according to Magg et al. (2022) with total metallicity $Z = 0.02$, and hydrogen abundance $X = 0.7$. Hedges & Madhusudhan (2016, see their Figure 2) carried out a thorough investigation to identify the relative dominance of pressure and Doppler broadening mechanisms in the pressure–temperature space. Following that analysis, we indicate an approximate limit above which molecular lines start to be broadened by pressure, resulting in a Lorentzian and/or Voigt profile (Burrows et al. 1998). We observe that only the top right corner of the opacity tables are affected by this phenomenon, whereas thermal Doppler is generally the main broadening mechanism. In terms of atomic opacities, we recall that we use monochromatic cross sections from the Opacity Project (Seaton et al. 1994), where line broadening is caused by pressure, radiation damping, and thermal Doppler effects.

Figure 3 illustrates a sample of condensed species for a scaled-solar composition with $\log(R) = -3$. Moving down to lower temperatures, the gas density ranges from 2.1×10^{-3} to 9.4×10^{-16} g cm^{-3}, while the gas pressure ranges from 3.8 to 3.2×10^{-6} dyn cm^{-2}. The general trends at a gas pressure of 1 bar are extensively discussed by Woitke et al. (2018). In this case, density and pressure are much lower, and condensation begins at lower temperatures. The first stable condensates to form are crystalline tungsten (W[s]) and baddeleyite (ZrO_2) at $T \simeq 1550$ K, corundum (Al_2O_3) at $T \simeq 1484$ K, perovskite ($CaTiO_3$) at $T \simeq 1386$ K, and gehlenite ($Ca_2Al_2SiO_7$) at $T \simeq 1326$ K. Below 1222 K, Al_2O_3 disappears and is replaced by the Ca-silicates group ($CaMgSi_2O_6$, $Ca_2Al_2SiO_7$, $CaAl_2Si_2O_8$, and $Ca_2MgSi_2O_7$), the titanates ($CaTiO_3$), and forsterite (Mg_2SiO_4). At and below a temperature of about 1125 K, silicates, iron condensates (Fe, FeS), and other species appear ($Al_6Si_2O_{13}$, Al_2SiO_5, $KAlSi_3O_8$ and $NaAlSi_3O_8$, Fe, $MgCr_2O_4$, $MgAl_2O_4$) and contribute the most to the grain abundance down to $T \simeq 160$ K. We note that at $T \simeq 400$ K halite (NaCl) starts to condense. At lower temperatures the element condensation is completed by one major species: water ice (H_2O) at $T \simeq 120$ K. At these low densities ammonia ice (NH_3) does not condense in appreciable amounts.

3. Opacity of Solid Grains

Computing the opacity caused by solid dust grains requires knowledge of the abundances of the different species as a function of temperature and density, as well as the absorption and scattering properties of each individual dust grain. The monochromatic cross section per unit mass (cm^2 g^{-1}) of a given solid species is calculated with

$$\kappa_\lambda^{\mathrm{grain}} = \frac{\int_{a_{\min}}^{a_{\max}} n(a) Q_{\mathrm{ext}}(a, \lambda) \pi a^2 \, da}{\rho}. \tag{2}$$

Here we assume that the grains are spherical particles with radius a and follow a power-law size distribution

$$n(a)da \propto a^{-\alpha}, \tag{3}$$

with $\alpha = 3.5$ discovered in the interstellar medium by Mathis et al. (1977, MRN). The lower and upper limits of the size distribution are set to $a_{\min} = 0.00625$ μm and $a_{\max} = 0.24$ μm, respectively, as determined by MRN for interstellar grains and also adopted by Ferguson et al. (2005). While an interstellar size distribution has been used as a standard in several studies, we recognize that it does not always apply in other physical situations. The total surface area of a dust species, which is proportional to its opacity, is highly dependent on $a_{\min}$. For instance, more appropriate parameters for modeling dust opacities

Table 1
Properties of Condensates

Condensate	Name	Group	ρ_d (g cm^{-3})	Optical Constants	λ (μm) Range	Analog
am-Al_2O_3	Corundum	Ox-/hydroxides	3.97	1,39	$0.2 \leqslant \lambda \leqslant 500$	
MgO	Periclase	Ox-/hydroxides	3.58	2	$0.016 \leqslant \lambda \leqslant 625$	
SiO	Silicon monoxide	Ox-/hydroxides	2.18	3,4	$0.05 \leqslant \lambda \leqslant 100$	
FeO	Ferropericlase	Ox-/hydroxides	5.99	5	$0.2 \leqslant \lambda \leqslant 500$	
Fe_2O_3	Hematite	Ox-/hydroxides	5.27	6	$0.1 \leqslant \lambda \leqslant 1000$	
Fe_3O_4	Magnetite	Ox-/hydroxides	5.20	6	$0.1 \leqslant \lambda \leqslant 1000$	
TiO_2	Rutile	Ox-/hydroxides	4.23	7,8,9	$0.4662 \leqslant \lambda \leqslant 36.2$	
ZrO_2	Baddeleyite	Ox-/hydroxides	5.68	10	$4.545 \leqslant \lambda \leqslant 25$	
$MgSiO_3$	Enstatite	Pyroxenes	3.19	11	$0.196 \leqslant \lambda \leqslant 9998$	
$NaAlSi_2O_6$	Jadeite	Pyroxenes	2.27	12	$6.69 \leqslant \lambda \leqslant 853$	
$NaAlSi_3O_8$	Albite	Feldspars	2.62	12	$6.69 \leqslant \lambda \leqslant 853$	
$Ca_2Al_2SiO_7$	Gehlenite	Melilites	3.04	12	$6.69 \leqslant \lambda \leqslant 853$	
$CaMgSi_2O_6$	Diopside	Pyroxenes	3.28	38	$7 \leqslant \lambda \leqslant 40$	
$CaMgC_2O_6$	Dolomite	Carbonates	2.86	13	$2.5 \leqslant \lambda \leqslant 50$	
$CaSiO_3$	Wollasnonite	Pyroxenoids	2.91	14	$0.00282 \leqslant \lambda \leqslant 6.198$	
Mg_2SiO_4	Forsterite	Olivines	3.21	11	$0.1957 \leqslant \lambda \leqslant 948$	
Ca_2SiO_4	Larnite	Nesosilicates	3.34			From Mg_2SiO_4
Fe_2SiO_4	Fayalite	Olivines	4.39	15	$0.4 \leqslant \lambda \leqslant 10{,}000$	
α-SiO_2	Quartz	Silicates	2.648	1,4	$6.67 \leqslant \lambda \leqslant 487.4$	
$MgAl_2O_4$	Spinel	Spinels	3.58	7,16	$0.35 \leqslant \lambda \leqslant 10{,}000$	
$CaTiO_3$	Perovskite	Perovskite	3.98	8,17	$0.0356 \leqslant \lambda \leqslant 5843$	
Na_2S	Sodium sulfide	Sulfides	1.86	18	$0.04 \leqslant \lambda \leqslant 200$	
FeS	Troilite	Sulfides	4.83	19,20	$0.1 \leqslant \lambda \leqslant 487$	
H_2O (ice)	Water	Ices	0.93	21	$0.0443 \leqslant \lambda \leqslant 2 \times 10^6$	
NH_3 (ice)	Ammonia	Ices	0.87	22	$2.5 \leqslant \lambda \leqslant 17$	
$MgTiO_3$	Geikeilite	Ilmenites	3.88	23	$0.25 \leqslant \lambda \leqslant 1$	
NaCl	Halite	Salts	2.165	24	$0.0477 \leqslant \lambda \leqslant 30{,}590$	
MnS	Alabandite	Rocksalts	4.08	25,26	$0.09 \leqslant \lambda \leqslant 190$	
KCl	Sylvite	Halides	1.99	27	$2 \leqslant \lambda \leqslant 1000$	
C	Graphite	C-rich matter	2.27	28	$0.0001 \leqslant \lambda \leqslant 123{,}984$	
am-C	Amorphous C	C-rich matter	2.27	29	$19.3 \leqslant \lambda \leqslant 50{,}119$	
SiC	Moissanite	Carbides	3.21	30	$0.001 \leqslant \lambda \leqslant 1000$	
TiC	Titanium carbide	Carbides	4.93	31,32	$0.015 \leqslant \lambda \leqslant 207$	
Ti	Titanium	Metals	4.14	33	$0.667 \leqslant \lambda \leqslant 200$	
Cr	Chromium	Metals	7.19	34,35	$0.04 \leqslant \lambda \leqslant 500$	
Mn	Manganese	Metals	7.43	13	$0.22 \leqslant \lambda \leqslant 55.6$	
Fe	Iron	Metals	7.87	35	$0.2 \leqslant \lambda \leqslant 285.7$	
Ni	Nickel	Metals	8.91	36	$0.667 \leqslant \lambda \leqslant 286$	
Cu	Copper	Metals	8.93	37	$0.517 \leqslant \lambda \leqslant 55.6$	
Zn	Zinc	Metals	7.14	13	$0.36 \leqslant \lambda \leqslant 55.6$	
Zr	Zirconium	Metals	6.52	13	$0.22 \leqslant \lambda \leqslant 55.6$	
W	Tungsten	Metals	19.25	33	$0.667 \leqslant \lambda \leqslant 200$	

Notes. Column (4) lists ρ_d, the specific density of the pure substance. In absence of optical constants we use data from analog species in column (7) as in Ferguson et al. (2005). The abbreviation am stands for amorphous. The optical constants for a few species are taken from Kitzmann & Heng (2017). The entire data set of optical constant can be collected from Zenodo: doi:10.5281/zenodo.8221361.

References. (1) Begemann et al. (1997); (2) Roessler & Huffman (1991); (3) Wetzel et al. (2013); (4) Philipp (1985); (5) Henning et al. (1995); (6) DOCCD Jena Laboratory; (7) Zeidler et al. (2011); (8) Posch et al. (2003); (9) Ribarsky (1997); (10) Dowling & Randall (1977); (11) Jäger et al. (2003); (12) Mutschke et al. (1998); (13) Querry (1987); (14) Edrees et al. (2018); (15) Fabian et al. (2001); (16) Tropf & Thomas (1991); (17) Ueda et al. (1998); (18) Khachai et al. (2009); (19) Henning & Mutschke (1997); (20) Pollack et al. (1994); (21) Warren (1984); (22) Hudson et al. (2022); (23) Hsiao et al. (2011); (24) Eldridge & Palik (1985); (25) Montaner et al. (1979); (26) Huffman & Wild (1967); (27) Palik (1985); (28) Draine (2003); (29) Jager et al. (1998); (30) Laor & Draine (1993); (31) Henning & Mutschke (2001); (32) Koide et al. (1990); (33) Ordal et al. (1988); (34) Rakic et al. (1998); (35) Lynch & Hunter (1991); (36) Ordal et al. (1987); (37) Ordal et al. (1985); (38) Arnold et al. (2014); (39) Koike et al. (1995).

in protoplanetary disks would be $a_{\rm min} = 0.1\ \mu$m and $a_{\rm max} = 3$ mm (Woitke et al. 2019). A simple application is discussed in Section 4.2. We also plan to vary the size range in follow-up works tailored to specific applications.

The dimensionless quantity $Q_{\rm ext}$ is the total extinction efficiency, which includes the absorption efficiency, $Q_{\rm abs}$, and the scattering efficiency, $Q_{\rm scat}$. The grain extinction efficiencies are calculated by applying Mie theory, the key component of which is the complex refractive index (or optical constants). The sources of optical constants, as well as other properties of dust grains, are listed in Table 1.

To compute $\kappa_\lambda^{\rm grain}$ of Equation (2), we use the DIANA Fortran package[8] (Woitke et al. 2016). DIANA is a versatile code with multiple entry options. One can specify the minimum and

[8] https://diana.iwf.oeaw.ac.at/

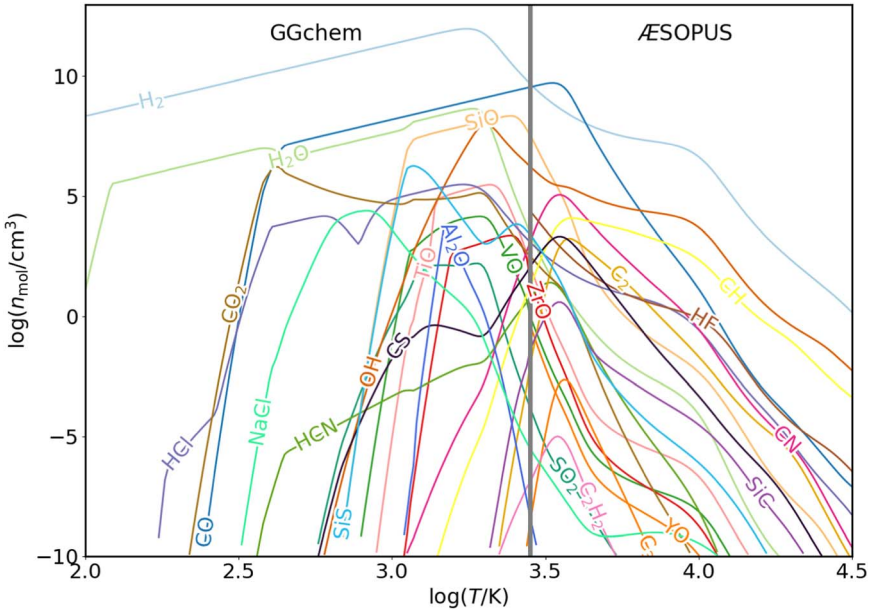

Figure 1. Abundances of a sample of molecules in the gas phase as a function of temperature, and for $\log(R) = -3$. The chemical composition assumes $X = 0.735$, $Z = 0.0165$, with scaled-solar elemental abundances according to Magg et al. (2022). The gray vertical line defines the transition temperature at $\log(T/\mathrm{K}) = 3.45$ between ÆSOPUS and GGchem.

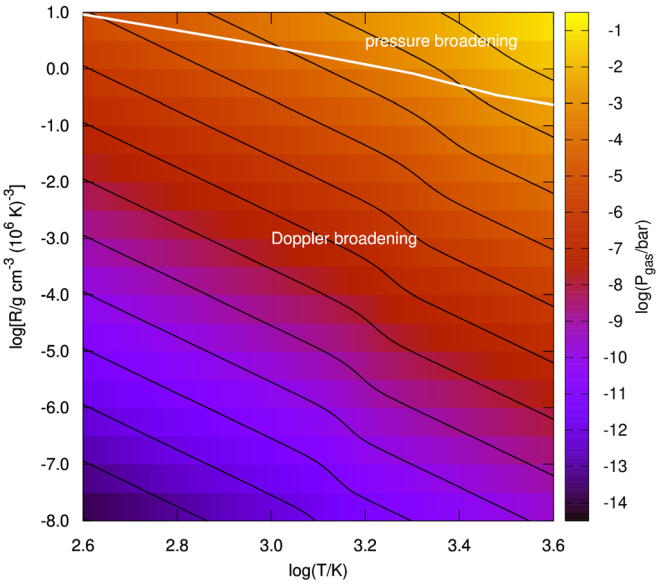

Figure 2. Map of gas pressure (bar) for temperatures $380 \lesssim T/\mathrm{K} \lesssim 4000$, where molecules and dust grains dominate the opacity. Contour levels (black lines) are distributed every 1 dex in $\log(P)$. The thick white line marks the boundary above which pressure broadening of molecular spectral absorption starts to affect the line wings (Hedges & Madhusudhan 2016). Below that line, the thermal Doppler effect can be safely assumed.

maximum sizes, $a_{\min}$ and $a_{\max}$, the power-law index α of the size distribution, the porosity P that defines the volume fraction of vacuum, and the distribution of hollow spheres (DHS) with a maximum hollow volume ratio $V_{\mathrm{hollow}}^{\max}$. As a starting choice we consider solid homogeneous spheres made of a single substance ($P = 0$, $V_{\mathrm{hollow}}^{\max} = 0$). Opacities with varying grain sizes, shapes, and porosities will also be analyzed in a follow-up work and can be incorporated upon user's request.

The monochromatic extinction profiles of the dust species included in ÆSOPUS 2.0 are depicted in Figure 4. Monatomic grains such as Fe, Cu, Cr, Ni, Zn, and Zr contribute scattering mainly at optical wavelengths, whereas corundum, spinel, perovskite, hematite, magnetite, dolomite, and gehlenite grains exhibit strong absorption peaks at infrared wavelengths.

4. Rosseland Mean Opacity

Updates in ÆSOPUS opacity. ÆSOPUS Rosseland mean opacities have previously been computed in the temperature range $1600 \lesssim T/\mathrm{K} \lesssim 30{,}000$. When the temperature is reduced to 400 K, the monochromatic opacities of the molecules must be expanded to cover the appropriate interval. The absorption data for 80 molecules in the gas phase are extended from $T = 100$ K to $T \simeq 30{,}000$ K. The adopted line lists are the EXOMOL database's recommended ones (Tennyson & Yurchenko 2012), with a few additions from HITRAN (Gordon et al. 2022). Table 2 of Marigo et al. (2022) contains the complete references but for one exception concerning ZrO opacity. We use the most recent ZorrO linelist (Perri et al. 2023), which has a temperature range of up to 10,000 K.

Molecular line profiles are treated with a thermal Doppler broadening plus a microturbulence velocity according to the following equations:

$$\phi(\nu) = \frac{1}{\Delta_\nu \sqrt{\pi}}\, e^{-\left(\frac{\nu-\nu_0}{\Delta_\nu}\right)^2}, \tag{4}$$

where ν_0 is the frequency of the line center, and Δ_ν is the line width, obtained with

$$\Delta_\nu = \frac{\nu_0}{c}\sqrt{\frac{2k_{\mathrm{B}}T}{m} + \xi^2}. \tag{5}$$

In this equation c stands for the speed of light, k_{B} for the Boltzmann constant, m for the molecule's mass, and ξ for the microturbolent velocity, which is set to 2.5 km s^{-1} (see Marigo & Aringer 2009; Marigo et al. 2022, for more details). In the range of pressures covered by our computations this should not significantly alter the Rosseland mean opacity (except for $0 \leqslant \log(R) \leqslant 1$; see Figure 2), given that the many different

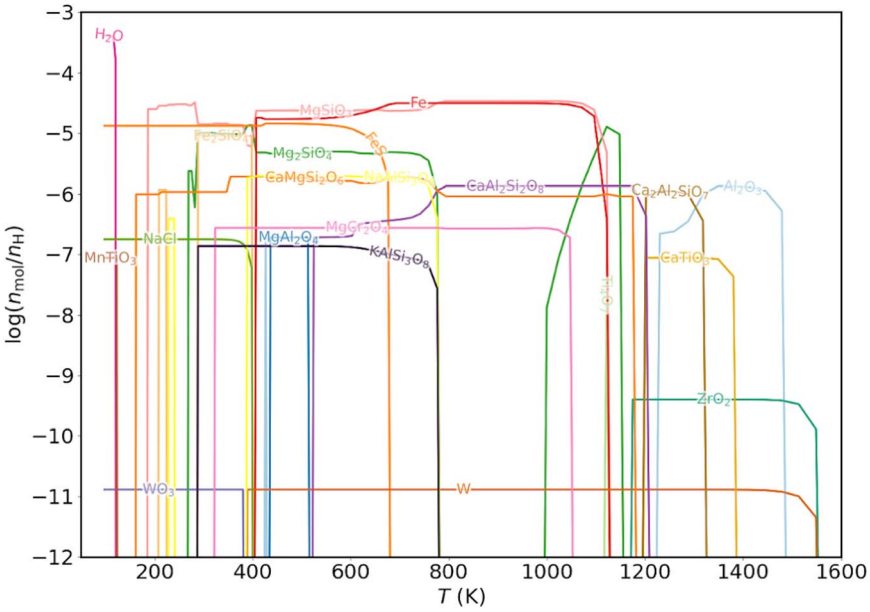

Figure 3. Onset of condensation as a function of temperature at $\log(R) = -3$, for solar abundances in phase equilibrium, computed with `GGchem`. The chemical composition is the same as in Figure 1. The plot depicts the abundances of several condensed species with respect to hydrogen nuclei.

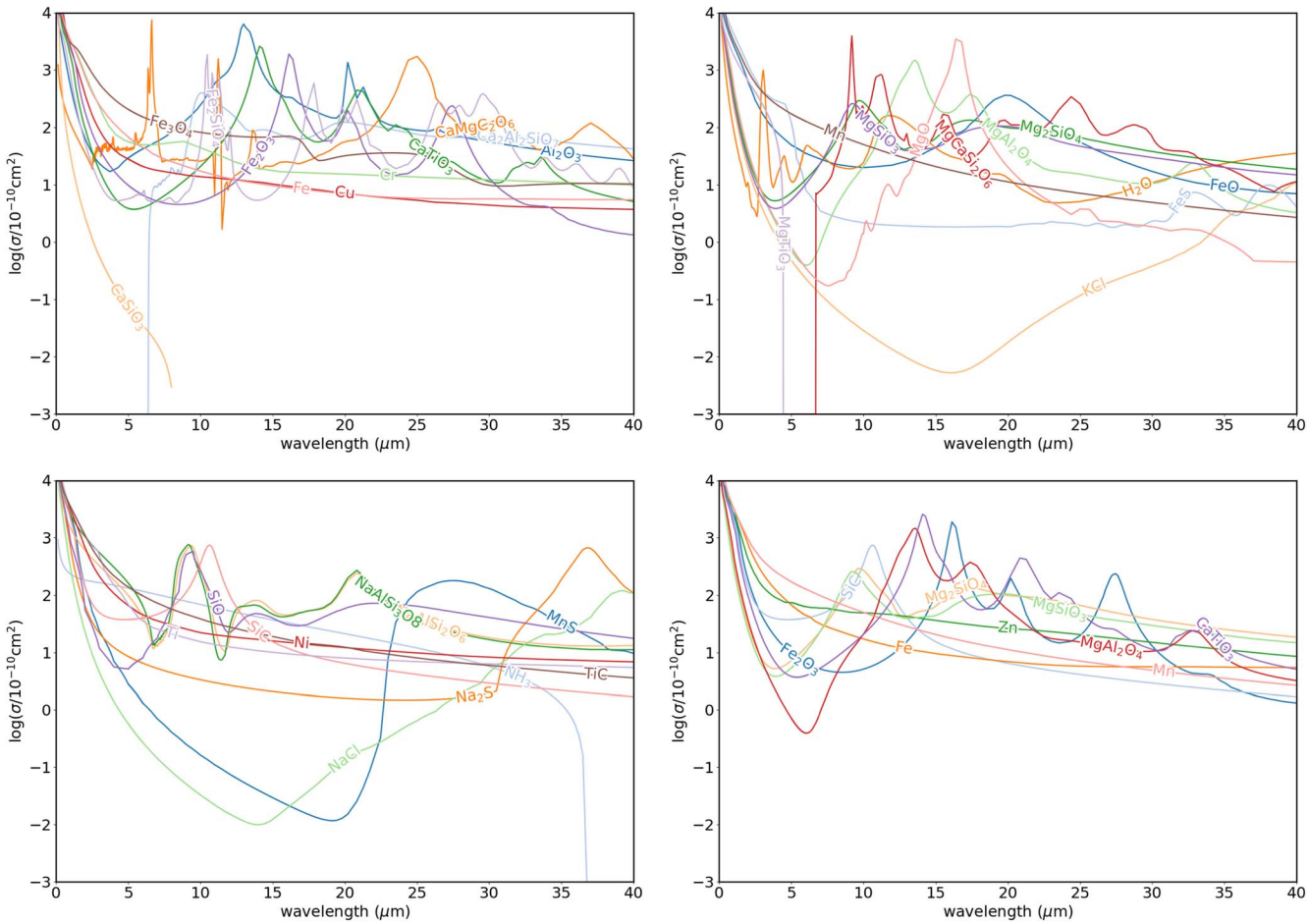

Figure 4. The average size-integrated extinction cross sections of various dust species made of a single substance. The Mie formalism is used, with diameters ranging from 0.00625 to 0.24 μm and assuming a power-law grain size distribution (see Equation (3)).

opacity sources overlap in ways that reduce the impact of ignoring the far wings of molecular transitions. Neglecting the line-extended wings could be severely incorrect in the case of planetary, brown dwarf, and very low-mass stellar atmospheres with little to no ionization and H primarily appearing in molecular form, H_2 (Burrows et al. 2001).

The method for calculating the Rosseland mean opacity is fully described in Marigo et al. (2022) and Marigo & Aringer (2009). To recap, for any selected (ρ, T) pair, we first compute the total monochromatic opacity cross section per unit mass (in $cm^2\ g^{-1}$), by including all the contributions from true absorption and scattering. The difference between this work and previous ones is that we now add $\kappa_\lambda^{\rm grain}$ of Equation (2). Second, we compute the Rosseland mean opacity, $\kappa_{\rm R}$ (in $cm^2\ g^{-1}$), by integrating over frequency:

$$\frac{1}{\kappa_{\rm R}(\rho, T)} = \frac{\int_0^\infty \frac{1}{\kappa(\nu)} \frac{\partial B_\nu}{\partial T} d\nu}{\int_0^\infty \frac{\partial B_\nu}{\partial T} d\nu}, \quad (6)$$

which is a harmonic weighted average with weights equal to the temperature derivatives of the Planck distribution, $\frac{\partial B_\nu}{\partial T}$. To set up the frequency grid we use the Helling & Jørgensen (1998) algorithm, which optimizes the frequency distribution in the opacity sampling technique (see the thorough discussion in Marigo et al. 2022).

The top panel of Figure 5 zooms in the temperature window where solid condensates dominate the Rosseland mean opacity. Similarly to Marigo et al. (2022) and Marigo & Aringer (2009), we show in the bottom panel of Figure 5 the quantity $\log(\kappa_{\rm R}) - \log(\kappa_{\rm R}^{i,\rm off})$ to highlight the temperature windows where the various opacity sources make a significant contribution. Here $\kappa_{\rm R}$ is the total Rosseland mean opacity including all opacity sources considered here, and $\kappa_{\rm R}^{i,\rm off}$ is the reduced opacity obtained by ignoring the species i, the role of which we intend to investigate.

We notice that $\kappa_{\rm R}$ has abrupt steep rises and drops, which correspond to sudden phase transitions/disappearances of various solid species. An opacity bump appears in the temperature range $1500 \gtrsim T/{\rm K} \gtrsim 1200$, which is caused primarily by the formation of corundum. At these temperatures, molecular band absorption by water continues to contribute, extending down to $\simeq$400 K. Perovskite is responsible for a small spike at $T \approx 1200$ K. For temperatures in the interval $1200 \gtrsim T/{\rm K} \gtrsim 400$ silicates and solid iron contribute most to $\kappa_{\rm R}$. At $T \simeq 1130$ K, forsterite makes a significant contribution. Finally, it is worth noting that amorphous carbon exhibits a moderate but discernible opacity bump in $\kappa_{\rm R}$ around $T \simeq 400$ K, in a mixture with solar composition.

4.1. Comparison with Other Authors

Figure 6 (left panel) shows a comparison of the results of this work and those of Ferguson et al. (2005) for a few values of the R parameter. There is a high degree of agreement down to $T \simeq 1600$ K. Below, in the regime of solid grains, differences begin to appear, involving primarily the opacity contributions of corundum, solid iron, and silicates. These differences could be attributed to different EoS solutions as well as differences in the complex refractive index of the various species. We note that our computations predict a higher $\kappa_{\rm R}$ produced by silicates. In the silicate regime ($T < 1500$ K), the opacity is slightly affected by the R parameter, whereas noticeable differences appear for the bump related to corundum (which condenses at lower temperatures as R decreases) and become more pronounced at higher temperatures. Another distinction is that we compute opacity down to $T \simeq 400$ K whereas Ferguson et al. (2005) stop at $T \simeq 500$ K.

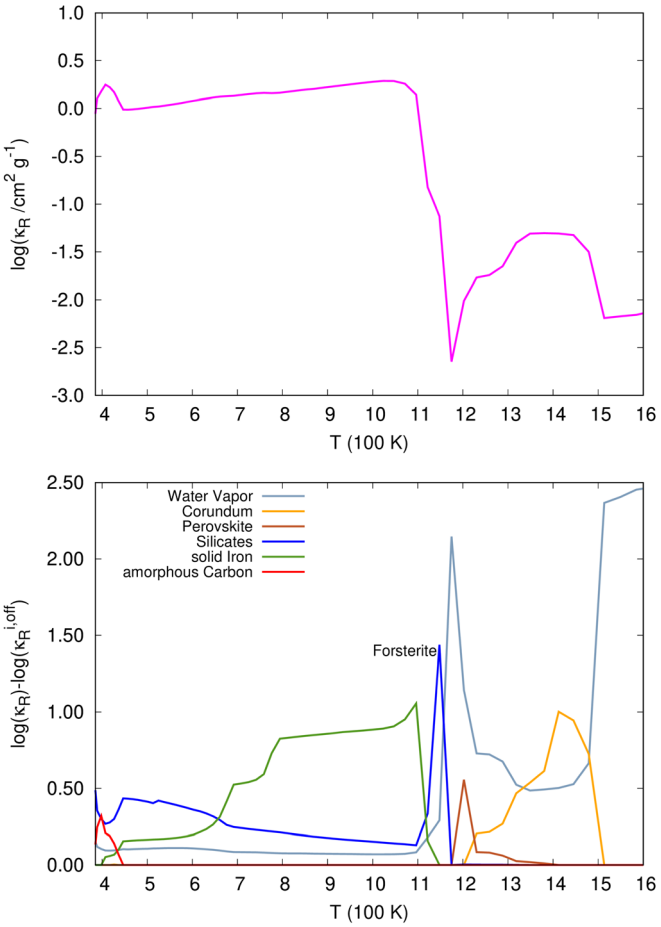

Figure 5. Properties of the Rosseland mean opacity in the low-temperature regime where solid species dominate. The chemical composition is defined by $X = 0.735$, $Z = 0.0165$, with scaled-solar elemental abundances following Magg et al. (2022). We take $\log(R) = -3$. Top panel: Rosseland mean opacity computed with ÆSOPUS 2.0. Bottom panel: contributions to the total Rosseland mean opacity of major solid species. Each curve corresponds to $\log(\kappa_{\rm R}) - \log(\kappa_{\rm R}^{i,\rm off})$, where $\kappa_{\rm R}$ is the full opacity including all opacity sources considered here, and $\kappa_{\rm R}^{i,\rm off}$ is the reduced opacity computed by omitting the specific absorbing species.

The right panel of Figure 6 compares the results of this work with those of Semenov et al. (2003). For this latter work, we use the open-source code[9] to compute $\kappa_{\rm R}$, and we use the assumptions of iron-poor silicates and dust grains considered as homogeneous spheres. Larger differences emerge in this case. First of all, we predict a higher water opacity bump at $T \simeq$ 2000 K, most likely due to the use of different line lists. Moreover, the absence of the opacity bump at $T \simeq 1500$ K in Semenov et al. (2003) is explained by the exclusion of high-temperature condensates, such as Al_2O_3. The discrepancy between the two opacity predictions becomes more pronounced at $T < 1000$ K. Several factors should be connected to the cause. While GGchem computes grain abundances for each combination of (T, ρ) in thermal equilibrium with the gas phase, Semenov et al. (2003) assumes some fixed abundances characteristic of protoplanetary disks (see also Pollack et al. 1994). Moreover, different approaches are used to define the condensation and vaporization temperatures. Furthermore, the size distribution functions of the grains in the two studies cover very different ranges. In this work we adopt

[9] https://www2.mpia-hd.mpg.de/~semenov/Opacities/opacities.html

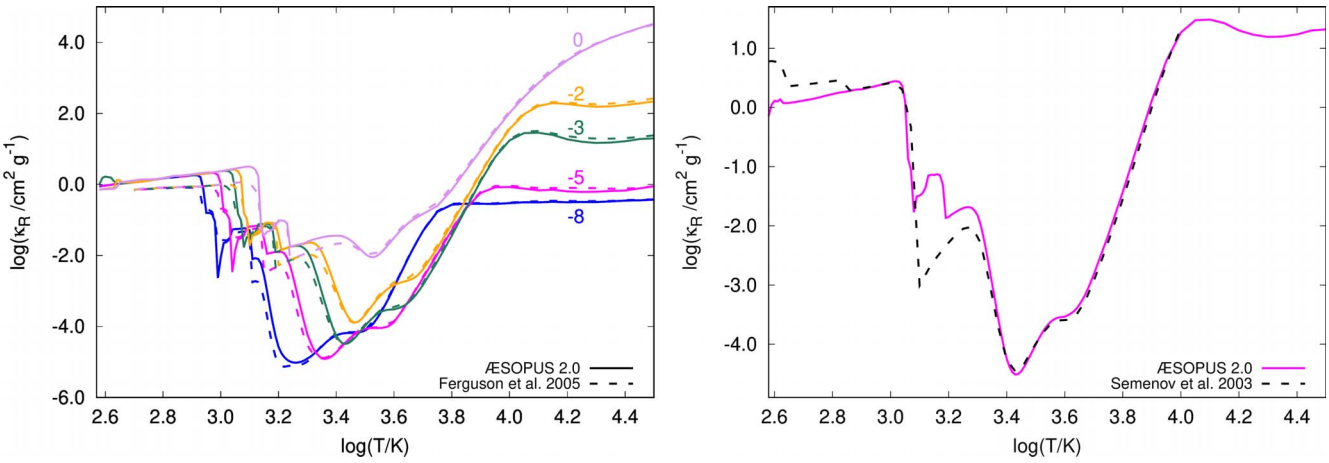

Figure 6. Comparison of Rosseland mean opacity between this work and other studies. Left panel: comparison with Ferguson et al. (2005). The chemical composition assumes $X = 0.7$, $Z = 0.02$, with scaled-solar elemental abundances according to Grevesse & Sauval (1998), for a few values of the $\log(R)$ parameter, which are labeled near the corresponding curves. Right panel: comparison with Semenov et al. (2003). The chemical mixture is defined by $X = 0.732$, $Z = 0.0194$, with scaled-solar elemental abundances according to Anders & Grevesse (1989). We take $\log(R) = -3$, which corresponds to a density range $10^{-13.2} \leqslant \rho/\mathrm{g\ cm^{-3}} \leqslant 10^{-7.5}$, moving from $\log(T/\mathrm{K}) = 2.6$ to $\log(T/\mathrm{K}) = 4.5$.

$a_{\rm min} = 0.00625\ \mu$m and $a_{\rm max} = 0.24\ \mu$m, whereas Semenov et al. (2003) take much larger grains, with $a_{\rm min} = 0.5\ \mu$m and $a_{\rm max} = 5\ \mu$m. Finally, different optical constants could be also a contributing factor.

4.2. Changing Dust Parameters: A Simple Application for Protoplanetary Disks

The opacity tables of this work are computed using a predefined set of physical assumptions for grain physics, based on the MRN study for interstellar grains, that may or may not be appropriate for specific applications. The DIANA package (Woitke et al. 2016) allows us to adjust our grain assumptions regarding size and its statistical distribution, porosity, and shape. Here we present a simple opacity test customized for the case of protoplanetary disks (proplyds). Following recent theoretical works on proplyds (Woitke et al. 2016, 2019) that reproduce continuum and line observations, we extract calibrated dust parameters. Specifically we set $a_{\rm min} = 0.1\ \mu$m, $a_{\rm max} = 3$ mm, porosity $P = 0.25$, and $V^{\rm max}_{\rm hollow} = 0.8$, and assume a power-law size distribution with $\alpha = 4$ (for a definition of the quantities, refer to Section 3). For this basic test we do not take dust-settling into account. Figure 7 (left panel) compares dust opacities computed according to MRN prescriptions for interstellar grains, and those suitable for proplyds. We note that Rosseland opacities for proplyds are much higher than those computed with MRN prescriptions, up to a factor of 5.6 in the temperature regime, below 1000 K, where silicates and iron dominate the opacity. We caution that the differences could be lessened by including dust-settling. To explain the reason, in the right panel of Figure 7 we compare the size-integrated cross sections as a function of wavelength. The curves exhibit variable trends, and cross sections for proplyds can be higher or lower than MRN cross sections in different wavelength ranges. However, using Wien's displacement law we can roughly estimate the peak wavelengths of the spectrum (black thick lines) at the typical temperatures where corundum ($1000 \lesssim T/\mathrm{K} \lesssim 2000$) and iron ($400 \lesssim T/\mathrm{K} \lesssim 1000$) contribute significantly to the opacity. This clarifies that proplyds have higher Rosseland mean opacities than MRN, because their cross sections are larger under these circumstances. Similar patterns are seen for silicates, as well as for the amorphous carbon opacity bump, particularly evident at $300 \lesssim T/\mathrm{K} \lesssim 400$ for $\rho = 10^{-15}$ g cm^{-3}.

4.3. Effects of Composition

Figure 8 (left panel) illustrates the impact of changes in metallicity on the Rosseland mean opacity. A scaled-solar composition is assumed in all cases except $Z = 0$, where no metals exist. As already noted by Ferguson et al. (2005), not only does the total opacity decrease as the amount of metals reduces, but condensation temperatures decrease as well, as fewer metals are available for the grains to exist in thermal equilibrium with. We also explore the effect on the opacity caused by chemical mixtures with various levels of alpha-enhancement, focusing especially on the temperature range where solid grains form (right panel of Figure 8). At constant metallicity, there are no dramatic changes in opacity, except in two temperature ranges. As $[\alpha/\mathrm{Fe}]$ increases, $\kappa_{\rm R}$ decreases for $300 \lesssim T/\mathrm{K} \lesssim 1000$, which is primarily due to a reduction in the abundance and hence opacity contribution of solid iron (see Figures 3 and 5). In a narrow temperature range around 125 K, we see a different pattern: the higher $[\alpha/\mathrm{Fe}]$, the greater the opacity. The increasing abundance of gehlenite ($Ca_2Al_2SiO_7$), which is composed of a few alpha-elements, explains this increment.

5. Rosseland Mean Opacity Tables with Solid Grains

We computed a standard set of opacity tables for the range $2.58 \leqslant \log(T/\mathrm{K}) \leqslant 4.5$ in 0.05 dex increments above $\log(T/\mathrm{K}) = 3.7$, while the temperature resolution is increased in 0.01 dex increments for $\log(T/\mathrm{K}) \leqslant 3.7$. This enables more accurate tabulation in regimes where opacity may undergo abrupt changes and discontinuities due to the dominating contribution of negative hydrogen ions, molecules, and solid grains. For the density parameter R we cover a range $-8 \leqslant \log(R) \leqslant 1$ in steps of 0.5 dex. Each table contains 129 temperature and 19 density points for a total of 2451 opacity values.

Opacity tables for other chemical compositions, or various choices of grain size, porosity, and shape, can be easily computed upon request. It should be noted that the effects of

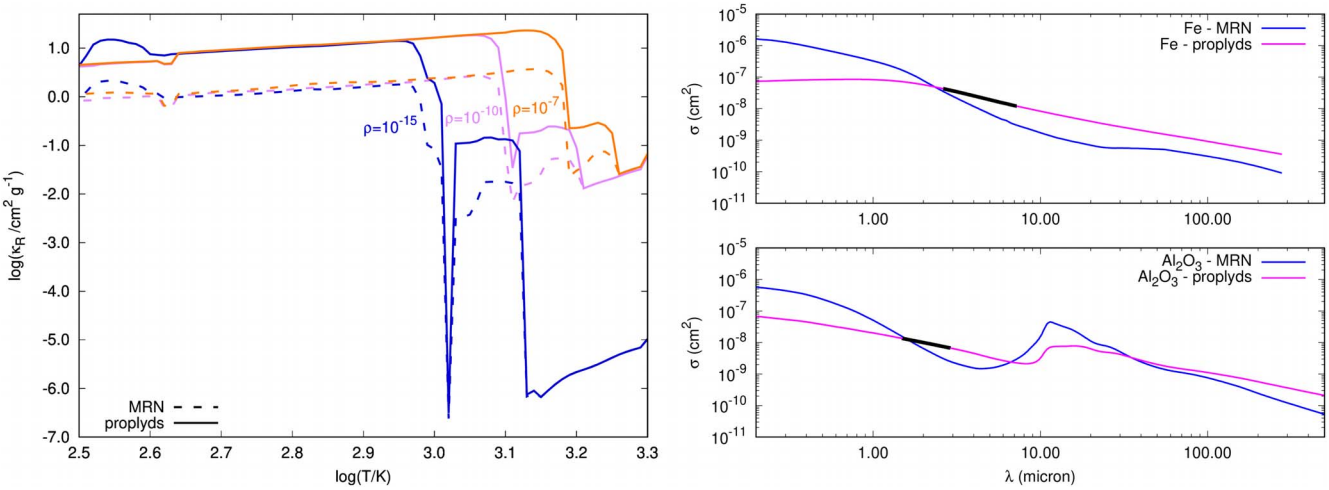

Figure 7. Left panel: Rosseland mean opacities in the dust regime computed with two different sets of assumptions: our standard choice based on MRN (dashed lines) and modified dust parameters appropriate for proplyds (solid lines). Each line represents a constant gas mass density within the range specified by Semenov et al. (2003). The chemical composition is scaled-solar according to Magg et al. (2022), with metallicity $Z = 0.02$ and hydrogen abundance $X = 0.7$. Right panel: size-integrated extinction cross sections for iron and corundum for two dust prescriptions examined in this work. According to Wien's displacement law, thick black lines correspond to the maximum wavelengths at the typical temperatures where the two dust species contribute most to the opacity. See text for more details.

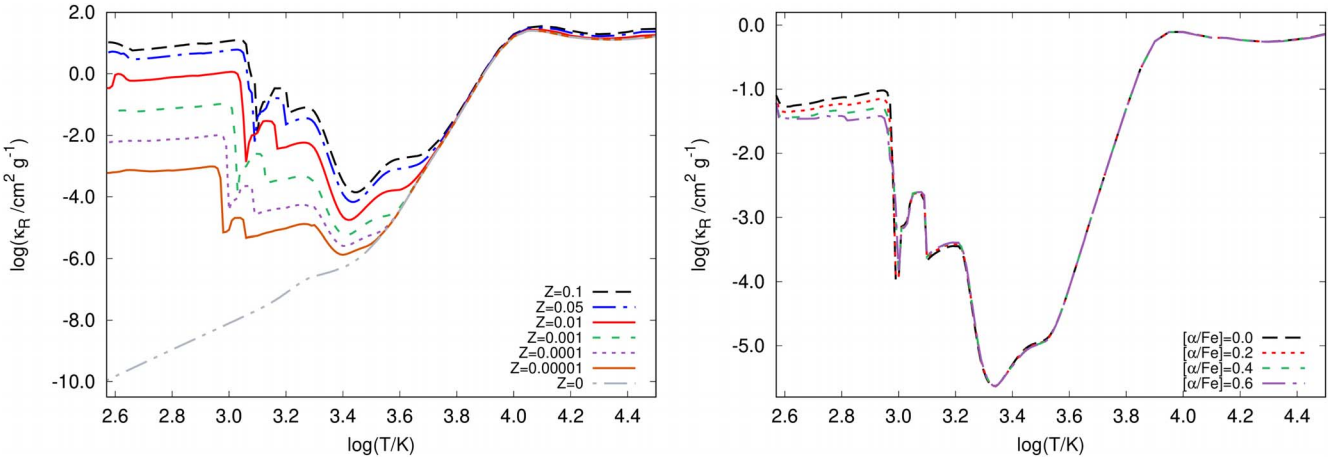

Figure 8. Properties of the Rosseland mean opacity as a function of chemical composition. The reference chemical mixture is defined by $X = 0.7$, with scaled-solar elemental abundances following Magg et al. (2022). Left panel: Rosseland mean opacity for several values of metallicity. We take $\log(R) = -3$. Right panel: Rosseland mean opacity for $Z = 0.001$ and a few degrees of alpha-enhancement, $[\alpha/\mathrm{Fe}]$. To maintain total metallicity, the increase in alpha-elements is balanced by a decrease in iron-group elements. We take $\log(R) = -5$.

changing the size distribution of dust grains, as well as their porosity and the presence of conglomerates of several dust species, have already been investigated by Ferguson et al. (2007). In particular, they find that "changing the distribution of grain size has a marginal effect on the total mean opacity". However, our investigation into the opacities for proplyds does not support this assertion.

6. Concluding Remarks

We compute the equation of state and provide Rosseland mean opacity tables for temperatures ranging from 30,000 K to 400 K with the inclusion of the opacity of several dust species, coupling the ÆSOPUS 2.0 and GGCHEM codes.

Due to the cost in computational time, especially at low temperatures where dust grains can form, we could not implement the real-time generation of opacity tables in the ÆSOPUS 2.0 web interface. Such an option is limited to the $3.2 \leqslant \log(T/\mathrm{K}) \leqslant 4.5$ temperature interval as described in Marigo et al. (2022). Nonetheless, users can retrieve Rosseland mean opacity tables extended to lower temperatures and optical constants of dust species from the repository at http://stev.oapd.inaf.it/aesopus_2.0/tables; copies of these files have also been deposited to Zenodo: doi:10.5281/zenodo.8221361.

The chemical distribution of the abundances follows a scaled-solar pattern, according to a few relevant solar mixtures in the literature. Below temperatures of ≃1500 K we include the opacity contribution of 43 solid grains. The grains are assumed to be homogeneous spheres, but other options for size, porosity, and shape may be considered in a future work and on user demand. Additionally, opacity tables for other underlying chemical compositions may be added to the repository based on user requirements. As an example, we present the opacities computed for a distribution with larger grains, more appropriate for the modeling of protoplanetary disks.

We recognize that in specific astrophysical environments, for instance for stars with powerful winds (asymptotic giant branch stars, red supergiants; Ferrarotti & Gail 2006; Höfner & Olofsson 2018) dust formation does not happen in equilibrium

as assumed here. Also dust-settling is a critical process in protoplanetary disks (Woitke et al. 2016). In a follow-up work we may address these aspects.

The opacity tables computed in this work are not suitable for very low-mass stars, brown dwarfs, and planets since the densities and gas pressures involved are typically too low for these cool objects. In this perspective we plan to expand the opacity tables at higher densities (with $\log(R) > 1$), where electron degeneracy and other nonideal effects, such as ionization potential depression, appear. Line pressure broadening should be considered in these conditions. This is crucial for modeling very low-mass stars, brown dwarfs, and planets.

Acknowledgments

This research is funded by the Italian Ministerial grant PRIN 2022, "Radiative opacities for astrophysical applications," no. 2022NEXMP8, CUP C53D23001220006. We also acknowledge support from Padova University through the research project PRD 2021. P.W. acknowledges funding from the European Union H2020-MSCA-ITN-2019 under grant Agreement no. 860470 (CHAMELEON).

Software: ÆSOPUS (Marigo & Aringer 2009; Marigo et al. 2022), ExoCross (Yurchenko et al. 2018), DIANA (Woitke et al. 2016), GGchem (Woitke et al. 2018), Opacity Project (Seaton et al. 1994).

ORCID iDs

Paola Marigo https://orcid.org/0000-0002-9137-0773
Peter Woitke https://orcid.org/0000-0002-8900-3667
Emanuele Tognelli https://orcid.org/0000-0001-5736-628X
Léo Girardi https://orcid.org/0000-0002-6301-3269
Bernhard Aringer https://orcid.org/0000-0001-9848-5410
Alessandro Bressan https://orcid.org/0000-0002-7922-8440

References

Alexander, D. R. 1975, ApJS, 29, 363
Alexander, D. R., & Ferguson, J. W. 1994, ApJ, 437, 879
Allard, F., Hauschildt, P. H., Alexander, D. R., & Starrfield, S. 1997, ARA&A, 35, 137
Allard, F., Hauschildt, P. H., Alexander, D. R., Tamanai, A., & Schweitzer, A. 2001, ApJ, 556, 357
Anders, E., & Grevesse, N. 1989, GeCoA, 53, 197
Arnold, J. A., Glotch, T. D., & Plonka, A. M. 2014, AmMin, 99, 1942
Begemann, B., Dorschner, J., Henning, T., et al. 1997, ApJ, 476, 199
Beichman, C., Benneke, B., Knutson, H., et al. 2014, PASP, 126, 1134
Birkby, J. L., de Kok, R. J., Brogi, M., Schwarz, H., & Snellen, I. A. G. 2017, AJ, 153, 138
Burrows, A., Hubbard, W. B., Lunine, J. I., & Liebert, J. 2001, RvMP, 73, 719
Burrows, A., Sudarsky, D., Sharp, C., et al. 1998, in ASP Conf. Ser. 134, Brown Dwarfs and Extrasolar Planets, ed. R. Rebolo, E. L. Martin, & M. R. Zapatero Osorio (San Francisco, CA: ASP), 354
Cushing, M. C., Marley, M. S., Saumon, D., et al. 2008, ApJ, 678, 1372
Decin, L., Richards, A. M. S., Waters, L. B. F. M., et al. 2017, A&A, 608, A55
Dowling, J. M., & Randall, C. 1977, Infrared Emissivities of Micron-Sized Particles of C, MgO, Al_2O_3, and ZrO_2 Tech. Rep., El Segundo: Aerospace Corp.
Draine, B. T. 2003, ApJ, 598, 1017
Edrees, S. J., Shukur, M. M., & Obeid, M. M. 2018, Comput. Condens. Matter, 14, 20
Eldridge, J., & Palik, E. 1985, in Handbook of Optical Constants of Solids, ed. E. D. Palik (New York: Academic), 775
Fabian, D., Henning, T., Jäger, C., et al. 2001, A&A, 378, 228
Ferguson, J. W., Alexander, D. R., Allard, F., et al. 2005, ApJ, 623, 585
Ferguson, J. W., Heffner-Wong, A., Penley, J. J., Barman, T. S., & Alexander, D. R. 2007, ApJ, 666, 261
Ferrarotti, A. S., & Gail, H. P. 2006, A&A, 447, 553
Fraine, J., Deming, D., Benneke, B., et al. 2014, Natur, 513, 526
Freedman, R. S., Marley, M. S., & Lodders, K. 2008, ApJS, 174, 504
Gordon, I., Rothman, L., Hargreaves, R., et al. 2022, JQSRT, 277, 107949
Grevesse, N., & Sauval, A. J. 1998, SSRv, 85, 161
Hedges, C., & Madhusudhan, N. 2016, MNRAS, 458, 1427
Helling, C., & Casewell, S. 2014, A&ARv, 22, 80
Helling, C., & Jørgensen, U. G. 1998, A&A, 337, 477
Henning, T., Begemann, B., Mutschke, H., & Dorschner, J. 1995, A&AS, 112, 143
Henning, T., & Mutschke, H. 1997, A&A, 327, 743
Henning, T., & Mutschke, H. 2001, AcSpA, 57, 815
Höfner, S., & Olofsson, H. 2018, A&ARv, 26, 1
Hsiao, C. Y., Shih, C. F., Chien, C. H., & Huang, C. 2011, JACS, 94, 363
Hudson, R. L., Gerakines, P. A., & Yarnall, Y. Y. 2022, ApJ, 925, 156
Huffman, D. R., & Wild, R. L. 1967, PhRv, 156, 989
Jäger, C., Fabian, D., Schrempel, F., et al. 2003, A&A, 401, 57
Jager, C., Mutschke, H., & Henning, T. 1998, A&A, 332, 291
Khachai, H., Khenata, R., Bouhemadou, A., et al. 2009, JPCM, 21, 095404
Kitzmann, D., & Heng, K. 2017, MNRAS, 475, 94
Koide, T., Shidara, T., Fukutani, H., et al. 1990, PhRvB, 42, 4979
Koike, C., Kaito, C., Yamamoto, T., et al. 1995, Icar, 114, 203
Laor, A., & Draine, B. T. 1993, ApJ, 402, 441
Lynch, D., & Hunter, R. 1991, in Handbook of Optical Constants of Solids II, ed. E. D. Palik (New York: Academic), 341
Magg, E., Bergemann, M., Serenelli, A., et al. 2022, A&A, 661, A140
Marigo, P., & Aringer, B. 2009, A&A, 508, 1539
Marigo, P., Aringer, B., Girardi, L., & Bressan, A. 2022, ApJ, 940, 129
Marley, M. S. 1998, in ASP Conf. Ser. 134, Brown Dwarfs and Extrasolar Planets, ed. R. Rebolo, E. L. Martin, & M. R. Zapatero Osorio (San Francisco, CA: ASP), 383
Mathis, J. S., Rumpl, W., & Nordsieck, K. H. 1977, ApJ, 217, 425
Montaner, A., Galtier, M., Benoit, C., & Bill, H. 1979, PSSAR, 52, 597
Mutschke, H., Begemann, B., Dorschner, J., et al. 1998, A&A, 333, 188
Ordal, M. A., Bell, R. J., Alexander, R. W., Long, L. L., & Querry, M. R. 1985, ApOpt, 24, 4493
Ordal, M. A., Bell, R. J., Alexander, R. W., Long, L. L., & Querry, M. R. 1987, ApOpt, 26, 744
Ordal, M. A., Bell, R. J., Alexander, R. W., Newquist, L. A., & Querry, M. R. 1988, ApOpt, 27, 1203
Palik, E. D. 1985, Handbook of Optical Constants of Solids (New York: Academic)
Perri, A. N., Taher, F., & McKemmish, L. K. 2023, MNRAS, 524, 4631
Philipp, H. R. 1985, in Handbook of Optical Constants of Solids, ed. E. D. Palik (New York: Academic), 719
Pollack, J. B., Hollenbach, D., Beckwith, S., et al. 1994, ApJ, 421, 615
Posch, T., Kerschbaum, F., Fabian, D., et al. 2003, ApJS, 149, 437
Querry, M. 1987, Optical Constants of Minerals and Other Materials from the Millimeter to the Ultraviolet Tech. Rep., Aberdeen: Chemical Research Develpment and Engineering Center
Rakic, A. D., Djurisic, A. B., Elazar, J. M., & Majewski, M. L. 1998, ApOpt, 37, 5271
Ramstedt, S., & Olofsson, H. 2014, A&A, 566, A145
Ramstedt, S., Vlemmings, W. H. T., Doan, L., et al. 2020, A&A, 640, A133
Rauer, H., Aerts, C., Cabrera, J. & PLATO Team 2016, AN, 337, 961
Ribarsky, M. 1997, in Handbook of Optical Constants of Solids, ed. E. D. Palik (New York: Academic), 795
Roessler, D. M., & Huffman, D. R. 1991, in Handbook of Optical Constants of Solids II, ed. E. D. Palik (New York: Academic), 951
Seaton, M. J., Yan, Y., Mihalas, D., & Pradhan, A. K. 1994, MNRAS, 266, 805
Semenov, D., Henning, T., Helling, C., Ilgner, M., & Sedlmayr, E. 2003, A&A, 410, 611
Tennyson, J., & Yurchenko, S. N. 2012, MNRAS, 425, 21
Tropf, W. J., & Thomas, M. E. 1991, in Handbook of Optical Constants of Solids II, ed. E. D. Palik (New York: Academic), 883
Ueda, K., Yanagi, H., Noshiro, R., Hosono, H., & Kawazoe, H. 1998, JPCM, 10, 3669
Warren, S. G. 1984, ApOpt, 23, 1206
Wetzel, S., Klevenz, M., Gail, H. P., Pucci, A., & Trieloff, M. 2013, A&A, 553, A92
Woitke, P., Helling, C., Hunter, G. H., et al. 2018, A&A, 614, A1
Woitke, P., Kamp, I., Antonellini, S., et al. 2019, PASP, 131, 064301
Woitke, P., Min, M., Pinte, C., et al. 2016, A&A, 586, A103
Yurchenko, S. N., Al-Refaie, A. F., & Tennyson, J. 2018, A&A, 614, A131
Zeidler, S., Posch, T., Mutschke, H., Richter, H., & Wehrhan, O. 2011, A&A, 526, A68